Medicine®

OPEN

Predictive models composed by radiomic features extracted from multi-detector computed tomography images for predicting low- and high- grade clear cell renal cell carcinoma
A STARD-compliant article

Xiaopeng He, MD[a,b], Hanmei Zhang, MD[a], Tong Zhang, MD[a], Fugang Han, MD[b], Bin Song, MD[a,*]

Abstract

To evaluate the values of conventional image features (CIFs) and radiomic features (RFs) extracted from multi-detector computed tomography (MDCT) images for predicting low- and high-grade clear cell renal cell carcinoma (ccRCC).

Two hundred twenty-seven patients with ccRCC were retrospectively recruited. Five hundred seventy features including 14 CIFs and 556 RFs were extracted from MDCT images of each ccRCC. The CIFs were extracted manually and RFs by the free software—MaZda. Least absolute shrinkage and selection operator (Lasso) was applied to shrink the high-dimensional data set and select the features. Five predictive models for predicting low- and high-grade ccRCC were constructed by the selected CIFs and RFs. The 5 models were as follows: model of minimum mean squared error (minMSE) of CIFs (CIF-minMSE), minMSE of cortico-medullary phase (CMP) of kidney (CMP-minMSE), minMSE of parenchyma phase (PP) of kidney (PP-minMSE), the combined model of CIF-minMSE and CMP-minMSE (CIF-CMP-minMSE), and the combined model of CIF-minMSE and PP-minMSE (CIF-PP-minMSE). The Lasso regression equation of each model was constructed, and the predictive values were calculated. The receiver operating characteristic (ROC) curves of predictive values of the 5 models were drawn by SPSS19.0, and the areas under the curves (AUCs) were calculated.

According to Lasso regression, 12, 19 and 10 features were respectively selected from the CIFs, RFs of CMP image and that of PP images to construct the 5 predictive models. The models ordered by their AUCs from large to small were CIF-CMP-minMSE (AUC: 0.986), CIF-PP-minMSE (AUC: 0.981), CIF-minMSE (AUC: 0.980), CMP-minMSE (AUC: 0.975), and PP-minMSE (AUC: 0.963). The maximum diameter of the largest axial section of ccRCC had a maximum weight in predicting the grade of ccRCC among all the features, and its cutoff value was 6.15 cm with a sensitivity of 0.901, a specificity of 0.963, and an AUC of 0.975.

When combined with CIFs, RFs extracted from MDCT images contributed to the larger AUC of the predictive model, but were less valuable than CIFs when used alone. The CIF-CMP-minMSE was the optimal predictive model. The maximum diameter of the largest axial section of ccRCC had the largest weight in all features.

Abbreviations: ARM = auto-regressive model, AUC = area under curve, ccRCC = clear cell renal cell carcinoma, CIF = conventional image feature, CIF-CMP-minMSE = combined model of CIF-minMSE and CMP-minMSE, CIF-minMSE = minimum mean squared error model of CIF, CIF-PP-minMSE = combined model of CIF-minMSE and PP-minMSE, CMP = cortico-medullary phase of kidney, CMP-minMSE = minimum mean squared error model of CMP, CSS = cancer specific survival, CT = computed tomography, GLCM = gray level co-occurrence matrix, GLH = gray level histogram, GLRLM = gray level run long matrix, HOG = histogram of oriented gradient, Lasso = least absolute shrinkage and selection operator, MDCT = multi-detector computed tomography, minMSE = minimum mean squared error model, NCP = non-contrast phase of kidney, PP = parenchyma phase of kidney, PP-minMSE = minimum mean squared error model of PP, RCC = renal cell carcinoma, RF = radiomic feature, ROC = receiver operating characteristic, WHO/ISUP = World Health Organization/International Society of Urological Pathology, WT = wavelet transformation.

Keywords: clear cell renal cell carcinoma, computed tomography, radiomic feature, radiomics

1. Introduction

Renal cell carcinoma (RCC) is the most common malignant tumor among the diseases of urinary system, accounting for about 85% of renal malignant tumors and 3% of body tumors. Clear cell renal cell carcinoma (ccRCC) is the most common subtype of RCC, accounting for about 70 to 80% of all kidney cancers.[1,2] The latest WHO/ISUP (World Health Organization/ International Society of Urological Pathology) grading system of RCC, with 4 stratifications (grade 1–4), is commonly used for evaluating the outcome of ccRCC and papillary RCC.[3,4] Many studies found that the WHO/ISUP grade of ccRCC was closely correlation with the cancer specific survival (CSS) of the patient and drew a conclusion that the higher WHO/ISUP grade the lower CSS could be got.[5–7] Kuthi et al[8] found the 5-year survival rate of grade 1 or 2 ccRCC was significant better than that of grade 3 or 4. However, there were not significant differences between the 5-year CSSs of grade 1 vs grade 2 tumors ($P = .550$), and that of grade 3 vs grade 4 tumors ($P = .226$). They also found when the grade 1 and 2 were combined into low-grade group, and the grade 3 and 4 into high-grade group, the 5-year CSSs of the 2 groups revealed a significant difference ($P < .0001$). The similar results could also be found in some other studies.[9–11] Preoperative needle biopsy and pathological section of the nidus are the most authoritative methods to determine the WHO/ISUP grade of ccRCC. However, their applications are limited due to their invasiveness. So, we aim to find if there is a noninvasive way to predict the pathological grade of ccRCC.

With the rapid development of medical imaging technology and equipment, especially the application of 64 or more rows multi-detector computed tomography (MDCT), the CT images with high isotropic resolution can be achieved, more precisely presenting the internal structure of lesion. Normally, we can perceive the information about size, shape, density, necrosis and blood supply of the lesions by naked eyes, but cannot for the RFs concealed in the MDCT images. The RF is a kind of feature reflecting the homogeneous phenomenon about the pixels in an image and can be quantitative analyzed by some special software.[12] Since 'Beyond Imaging' was selected as the theme of the 2016 annual conference of the Radiological Society of North America (RSNA), the radiomics has become a buzzword now. It refers to the high-throughput extracting of massive imaging features describing the characteristics of the pixels of nidus in digital medical images.[13] In a short time, a large number of studies about radiomics emerged, mainly focusing on preoperative accurate diagnosis, classifying, and prognosis of tumors.[14–17]

Owing to obvious characteristics on enhanced CT images, such as fast in and out style of enhancement in artery phase and polycystic necrosis, ccRCC can be differentiated from the other subtypes of RCC, such as papillary RCC, chromophobe RCC, and oncocytoma, without much difficulty.[18] With the development of precision medicine and personalized treatment, more and more clinicians want to know the WHO/ISUP grade of ccCC before treatment or operation, in order to determine the way of therapy and roughly predict the cancer-free survival (CSS) if surgery. Though, there were some radiomic studies about ccRCC could be found, however, their RFs were drown mainly from gray level histograms (GLH) and the outdated Fuhrman grading system of RCC was referred.[19–23] As far as we know, there are no radioimc studies about exploring the correlations between numerous RFs and WHO/ISUP grades of ccRCC. So, we conduct this study with an intention to uncover the relationships between the RFs and the WHO/ISUP grades of ccRCC.

The whole procedure of this research included 4 parts: extracting massive RFs from MDCT images; selecting the most predictive RFs by Lasso regression and then constructing 5 predictive models; using the predictive models to calculate the predictive value for each ccRCC; and drawing ROC curves of the predictive values, calculating the AUC and the cutoff value of each model. Our ultimate aim is to find the optimal predictive model composed by CIFs and RFs for recognizing low-grade (WHO/ISUP grade 1 and 2) and high-grade (WHO/ISUP grade 3 and 4) ccRCC.

2. Materials and methods

2.1. Patients

This study was a retrospective case-control investigation, approved by the Ethics Committee of Sichuan University, and the consents from patients were waived. Two hundred seventy-one patients with ccRCC confirmed by 2 pathologists through biopsy or surgical resection were searched from the picture archiving and communication system (PACS) of our hospital from January 2012 to June 2017. The inclusion criteria of cases were as follows: no previous treatment in the patients before CT examination; the MDCT scanning of the patient must comprise 3 phases [the non-contrast phase (NCP), the cortico-medullary phase (CMP), and the parenchyma phase (PP) of enhanced CT scanning]; every case must has an explicit WHO/ISUP grade confirmed by pathology. Overall, in this study, 7 cases were excluded for having previous treatments, 16 cases were excluded for inadequate phases of MDCT scanning, and 21 cases were excluded for non-explicit WHO/ISUP grades. Finally, 227 patients remained in this study, of which 130 cases were male patients, 97 cases were female patients, the age range was 10 to 85 years old, the mean age was 57.3 ± 12.9 years, 136 cases were low-grade ccRCCs (WHO/ISUP grades 1 and 2), and 91 cases were high-grade ccRCCs (WHO/ISUP grades 3 and 4) (Table 1).

2.2. CT acquisition

Two hundred and four patients were examined by a 64-multidetector spiral CT scanner (LightSpeed VCT, GE Health-care), and 23 patients were examined by a 256-multidetector

Table 1

Demographic and clinical characteristics of patients with clear cell renal cell carcinoma (ccRCC).

Characteristic of ccRCC	Data of ccRCC
Gender	
Male	130 (60.4%)
Female	97 (39.6%)
Age (y)	
Median (y)	57.3 ± 12.9
Range (y)	10–85
≤ 50	71 (31.2%)
51–69	115 (50.7%)
≥ 70	41 (18.1%)
WHO/ISUP grade	
1	69 (30.4%)
2	67 (29.5%)
3	39 (17.2%)
4	52 (22.9%)

ccRCC = clear cell renal cell carcinoma.

spiral CT scanner (Brilliance iCT, Philips Healthcare). The NCP, CMP, and PP were recorded in each patient. The scanning protocols of the 3 phases were as follows: using spiral scanning and thin-slice reconstruction in NCP, CMP, and PP; the scanning of CMP and PP were started at 30th and 90th second after the contrast agent was injected into the antecubital vein, respectively. Contrast agent (70–100 mL; Iopamiro, Bracco, Italy; Ultravist, Bayer, Germany) was injected into the antecubital vein by high pressure injector at a rate of 3.5 ml/s. The CT scanning parameters of the 3 phases were as follows: the tube voltage was 120 KV; the automated tube-current modulation based on weight was used; collimation width was 0.625 mm; the pitch was 0.967:1; the reconstruction thickness was 1.5 to 2.5 mm; the field of view (FOV) was 360 mm; and the matrix was 512×512.

2.3. Conventional image features (CIFs) acquisition

The CIFs were extracted from MDCT images in the PACS (Huahai Health, China) of our hospital by 2 radiologists with 10 and 15 years of experience in diagnosis of abdominal imaging, respectively, both blinded to the explicit WHO/ISUP grade of each ccRCC. The region of interest (ROI) was determined according to the consents of the 2 radiologists. When measuring the attenuation of the parenchyma of ccRCC, they put 3 ROIs with the areas from 2.0 to 5.0 cm^2, and then took the mean attenuation of the 3 ROIs for study. When measuring the whole attenuation of the maximum axial section of ccRCC including the necrotic area, the contour of the ROI was recessed approximately 2 mm from the tumor margin to reduce the partial volume effect. In this study, the CIFs defined and consented by the 2 radiologists were presented in Table 2.

Table 2

List of the conventional image features (CIFs) extracted from multi-detector computed tomography (MDCT) images of each clear cell renal cell carcinoma (ccRCC).

The name of CIF	The definition of CIF
X1	Age of each patient with ccRCC
X2	Attenuation of parenchyma of ccRCC on NCP
X3	Attenuation of parenchyma of ccRCC on CMP
X4	Attenuation of parenchyma of ccRCC on PP
X5	Mean attenuation of the maximum axial section of ccRCC including necrotic area on NCP
X6	Mean attenuation of the maximum axial section of ccRCC including necrotic area on CMP
X7	Mean attenuation of the maximum axial section of ccRCC including necrotic area on PP
X8	Area of the maximum axial section of ccRCC
X9	Maximum diameter of the maximum axial section of ccRCC
X10	The absolute enhanced attenuation (X3-X2) of parenchyma of ccRCC on CMP
X11	The absolute enhanced attenuation (X4-X2) of parenchyma of ccRCC on PP
X12	The homogeneity rate of the maximum axial section of ccRCC based on CT values (X5/X2) on NCP
X13	The homogeneity rate of the maximum axial section of ccRCC based on CT values (X6/X3) on CMP
X14	The homogeneity rate of the maximum axial section of ccRCC based on CT values (X7/X4) on PP

ccRCC = clear cell renal cell carcinoma, CIF = conventional image feature, CMP = cortico-medullary phase of kidney, NCP = non-contrast phase of kidney, PP = parenchyma phase of kidney, X10 = X3-X2; X11 = X4-X2; X12 = X5÷X2; X13 = X6÷X3; X14 = X7÷X4.

2.4. Radiomic feature (RF) extraction (Fig. 1)

Image selection: the images of the maximum axial section of each ccRCC on CMP and PP were chosen. All the images extracted from PACS were anonymized. The reconstructive thickness of each image was 1.5 to 2.5 mm. The window width and window level of every MDCT image ranged from 300 to 400 HU and 45 to 65 HU, respectively.

The ROI definition: The irregular contour of ROI drew by manually was recessed approximately 2 mm from the margin of tumor to reduce the interference by adjacent tissue, such as fat and normal renal tissue.

The RFs extraction: The RFs were extracted by a free software package, MaZda (version 4.6)[24,25] and primarily came from gray level histogram (GLH), gray level co-occurrence matrix (GLCM), gray level run long matrix (GLRLM), histogram of oriented gradient (HOG), wavelet transformation (WT), and auto-regressive model (ARM) of the MDCT images of each ccRCC. The RFs coming from GLH indicated the intensity distribution of image pixels, but without spatial information. The RFs deriving from GLCM indicated the changes of pixel signal intensities with the increase of pixel length and described the distributions of the pixels with the same gray level at different orientation. The RFs derived from GLRLM reflected the homogeneity of pixel gray levels in different directions. The RFs derived from HOG primarily reflected the contour information of the images. The RFs derived from WT indicated the frequencies of a certain cohort of pixel gray levels within images. The RFs deriving from ARM, in which the gray level of some pixel could be estimated by the neighboring pixels, manifested the homogeneity of image in some degree.[26,27] Overall, from the MDCT images of CMP and PP of each ccRCC, 556 RFs were extracted from the ROI of nidus in the maximum axial section.

2.5. Data standardization

To minimize the effects of variations of contrast and brightness of images, the gray level values of pixels were normalized by putting into the range of $\mu \pm 3\sigma$ (μ, mean gray level value; σ, standard deviation) before statistical analysis. The values of different kinds of RFs were normalized into the range (0, 1) by sigmoid function, respectively.

2.6. RFs screening and predictive model construction

The most predictive features among the primary dataset were selected by the least absolute shrinkage and selection operator (Lasso) regression, which is very suitable for the shrinkage of a high-dimensional dataset.[28] By means of Lasso regression, the minimum mean squared error model (minMSE) composed by the most predictive features was obtained from the dataset of CIFs, RFs of CMP, and that of PP, respectively. The 3 minMSEs were abbreviated as CIF-minMSE, CMP-minMSE, and PP-minMSE, respectively. The combined model of CIF-minMSE and CMP-minMSE was abbreviated as CIF-CMP-minMSE, and that of CIF-minMSE and PP-minMSE was abbreviated as CIF-PP-minMSE.

2.7. Statistical analysis

The Lasso regression equation of each model for predicting low- and high-grade ccRCC was constructed, and the predictive value
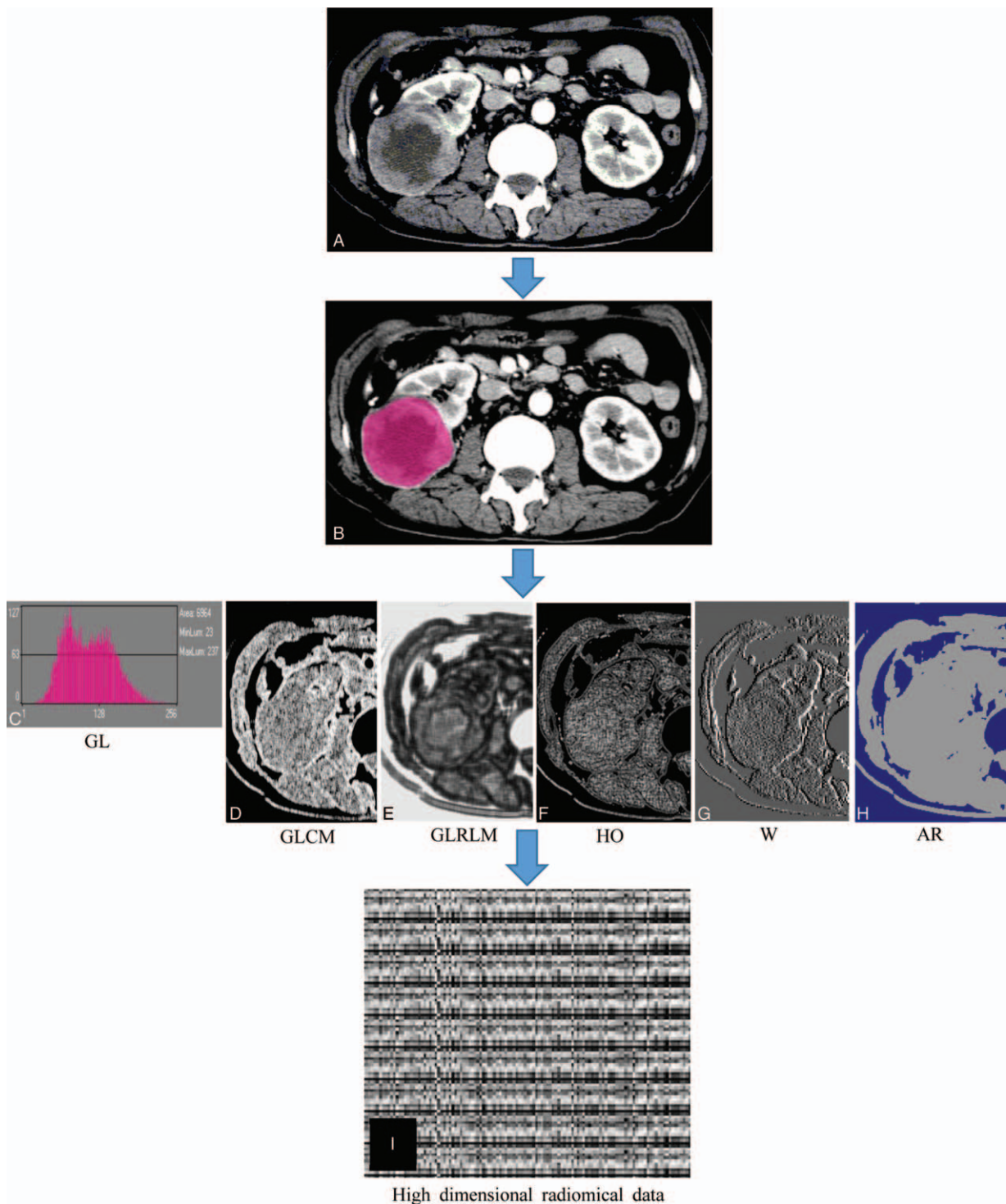
Figure 1. Flowchart of radiomic features (RFs) extraction from MDCT image. (A) The image of the maximum axial section of clear cell renal cell carcinoma (ccRCC) on cortico-medullary phase of kidney (CMP) was chosen. (B) The region of interest (ROI) of tumor was drown by pink color on MaZda (version 4.6). (C) The gray level histogram (GLH) of tumor was calculated. (D) The gray level co-occurrence matrix (GLCM) of tumor was calculated. (E) The gray level run long matrix (GLRLM) of tumor was calculated. (F) The histogram of oriented gradient (HOG) of tumor was calculated. (G) The wavelet transformation (WT) of tumor was calculated. (H) The auto-regressive model (ARM) of tumor was calculated. (I) The high dimensional radiomic data set of tumor was constructed. ARM = auto-regressive model, CMP = cortico-medullary phase of kidney, ccRCC = clear cell renal cell carcinoma, GLCM = gray level co-occurrence matrix, GLH = gray level histogram, GLRLM = gray level run long matrix, HOG = histogram of oriented gradient, MDCT = multi-detector computed tomography, RFs = radiomic features, ROI = region of interest, WT = wavelet transformation.

of each ccRCC ('1.0' defined as the standard value of low-grade ccRCC and '2.0' defined as the standard value of high-grade ccRCC) was calculated. The receiver operating characteristic (ROC) curve of predictive values of each model was drawn by SPSS19.0 (SPSS Inc., Chicago, IL), and the area under curve (AUC) was calculated.

3. Results

Twelve features were selected from CIFs by Lasso regression and constructed the model of minMSE. The equation of Lasso regression of CIF-minMSE was as follows: CIF-minMSE_Y = 0.1741*X1-0.0717*X3-0.1379*X4-0.2986*X5+0.8157*X6-0.6586*X8+2.4304*X9-0.5833*X10-0.0103*X11-0.0176*X12-0.3042*X13-0.2645*X14 (the '*' in the equation means 'multiply').

Nineteen features were selected from the 278 RFs extracted from CMP by Lasso regression and constructed the model of minMSE. The equation of Lasso regression of CMP-minMSE

Table 3

The definitions and interpretations of the radiomic features selected by Lasso regression from cortico-medullary phase of kidney (CMP) or parenchyma phase of kidney (PP).

Name of model	RFs selected by Lasso	Full name	Main meaning in the ROI	Which group belongs to	weight coefficient in the equation of Lasso regression
CMP-minMSE	Area	Area	Sum number of pixels	General feature	1.0192
	MinNorm	Minimum normalization	Value of minimum normalization	General feature	−0.2748
	Hist_Skewness	Histogram's skewness	Histogram's skewness	GLH	0.0493
	Hist_Perc.50%	50% percentile of histogram	50% percentile of histogram	GLH	−0.2055
	S(0,1)Entropy	S(0,1) entropy	Entropy of 1-pixel length in 90° orientation	GLCM	0.2595
	S(0,2)SumOfSqs	S(0,2) sum of squares	Sum of squares of 2-pixel length in 90° orientation	GLCM	−0.1400
	S(2,2)SumAverg	S(2,2) sum average	Sum average of 2-pixel length in 45° orientation	GLCM	0.0818
	S(3,3)Entropy	S(3,3) entropy	Entropy of 3-pixel length in 45° orientation	GLCM	0.2582
	S(4,0)SumEntrp	S(4,0) sum entropy	Sum entropy of 4-pixel length in 0° orientation	GLCM	0.0818
	S(5,0)InvDfMom	S(5,0) inverse difference moment	Inverse difference moment of 5-pixel length in 0° orientation	GLCM	0.3582
	S(5,−5)SumAverg	S(5,−5) sum average	Sum average of 5-pixel length in 135° orientation	GLCM	−0.0072
	Vertl_RLNonUni	Vertical run length nonuniformity	Run length nonuniformity in vertical direction	GLRLM	0.4781
	GrSkewness	Gradient skewness	Absolute gradient skewness	HOG	0.0187
	GrKurtosis	Gradient kurtosis	Absolute gradient kurtosis	HOG	0.0373
	Teta2	Teta2	1 pixel intensity can been best calculated by ARM using parametr θ_2	ARM	0.1331
	WavEnHL_s-1	Wavelet energy high low subband image 1	Energies of wavelet coefficients calculated in subband image 1 added high- and low-pass filters in row and column respectively	WT	−0.1561
	WavEnLL_s-3	Wavelet energy low low subband image 3	Energies of wavelet coefficients calculated in subband image 3 added low- and low-pass filters in row and column respectively	WT	0.2385
	WavEnHH_s-3	Wavelet energy high high subband image 3	Energies of wavelet coefficients calculated in subband image 3 added high- and high-pass filters in row and column respectively	WT	−0.0505
	WavEnLL_s-4	Wavelet energy low low subband image 4	Energies of wavelet coefficients calculated in subband image 4 added low- and low-pass filters in row and column respectively	WT	−0.1909
PP-minMSE	Area	Area	Sum number of pixels	General feature	0.1597
	MinNorm	Minimum normalization	Value of minimum normalization	General feature	−0.3982
	S(5,5)DifVarnc	S(5,5) difference variance	Difference variance of 5-pixel length in 45° orientation	GLCM	−0.1115
	S(5,−5)Entropy	S(5,−5) entropy	Entropy of 5-pixel length in 135° orientation	GLCM	0.1722
	S(5,−5)DifEntrp	S(5,−5) difference entropy	Difference entropy of 5-pixel length in 135° orientation	GLCM	−0.2169
	Vertl_RLNonUni	Vertical run length nonuniformity	Run length nonuniformity in vertical direction	GLRLM	1.4737
	Teta2	Teta2	1 pixel intensity can been best calculated by ARM using parametr θ_2	ARM	0.0308
	WavEnHL_s-2	Wavelet energy high low subband image2	Energies of wavelet coefficients calculated in subband image 2 added high- and low-pass filters in row and column respectively	WT	−0.0228
	WavEnLH_s-3	Wavelet energy low high subband image 3	Energies of wavelet coefficients calculated in subband image 3 added low- and high-pass filters in row and column respectively	WT	−0.0180
	WavEnHL_s-3	Wavelet energy high low subband image 3	Energies of wavelet coefficients calculated in subband image 3 added high- and low-pass filters in row and column respectively	WT	−0.0216

ARM = auto-regressive model, CMP = cortico-medullary phase of kidney, CMP-minMSEM = minMSE of CMP, GLCM = gray level co-occurrence matrix, GLH = gray level histogram, GLRLM = gray level run long matrix, HOG = histogram of oriented gradient, minMSEM = minimum mean squared error model, PP = parenchyma phase of kidney, PP-minMSEM = minMSE of PP, WT = wavelet transformation.

was as follows: CMP-minMSE_Y = 1.0192*Area-0.2748* MinNorm+0.0493*Hist_Skewness-0.2055*Hist_Perc.50% +0.2595*S(0,1)Entropy-0.1400*S(0,2)SumOfSqs+0.0818*S (2,2)SumAverg + 0.2582*S(3,3)Entropy+0.0818*S(4,0) SumEntrp+0.3582*S(5,0)InvDfMom-0.0072*S(5,-5)SumAverg +0.4781*Vertl_RLNonUni+0.0187*GrSkewness+0.0373* GrKurtosis+0.1331*Teta2-0.1561*WavEnHL_s-1+0.2385* WavEnLL_s-3-0.0505*WavEnHH_s-3-0.1909*WavEnLL_s-4.

Ten features were selected from the 278 RFs extracted from PP by Lasso regression and constructed the minMSE model. The equation of Lasso regression of PP-minMSE was as follows: PP-minMSE_Y=0.1597*Area -0.3982*MinNorm-0.1115*S(5,5) DifVarnc+0.1722*S(5,-5)Entropy-0.2169*S(5,-5)DifEntrp +1.4737*Vertl_RLNonUni+0.0308*Teta2-0.0228* WavEnHL_s-2-0.0180*WavEnLH_s-3-0.0216*WavEnHL_s-3.

In the Lasso equations of the models of CIF-minMSE, CMP-minMSE, and the PP-minMSE, we found the X1, X6, and X9 of CIFs, the Area, Skewness, S(0,1)Entropy, S(2,2)SumAverg, S(3,3) Entropy, S(4,0)SumEntrp, S(5,0)InvDfMom, Vertl_RLNonUni, GrSkewness, GrKurtosis,Teta2, and WavEnLL_s-3 of RFs from CMP, and the Area, S(5,-5)Entropy, Vertl_RLNonUni, and

Teta2 of RFs from PP had positive weight coefficients. However, the X3, X4, X5, X8, X10, X11, X12, X13, and X14 of CIFs, the MinNorm, Hist_Perc.50%, S(0,2)SumOfSqs, S(5,-5)SumAverg, WavEnHL_s-1, WavEnHH_s-3, and WavEnLL_s-4 of RFs from CMP, and the MinNorm, S(5,5)DifVarnc, S(5,-5)DifEntrp, WavEnHL_s-2,WavEnLH_s-3, and WavEnHL_s-3 of RFs from PP had negative weight coefficients. The definitions and interpretations of the RFs selected by Lasso regression and the groups that they belonged to was shown in Table 3.

The scattergram and histogram the predictive values of CIF-CMP-minMSE, for example, for predicting low- and high-grade ccRCC were shown in Figures 2 and 3, respectively. The cutoff values, sensitivities, specificities, and AUCs of the 5 predictive models (CIF-minMSE, CMP-minMSE, PP-minMSE, CIF-CMP-minMSE, and CIF-PP-minMSE) were shown in Table 4. The ROC curves of the 5 models were shown in Figure 4. In addition, the largest diameter of the maximum axial section of ccRCC (the X9 of CIFs) gained also good performance in predicting low- and high-grade ccRCC individually. Its cutoff value was 6.15 cm, with a sensitivity of 0.901, a specificity of 0.963, and an AUC of 0.975.
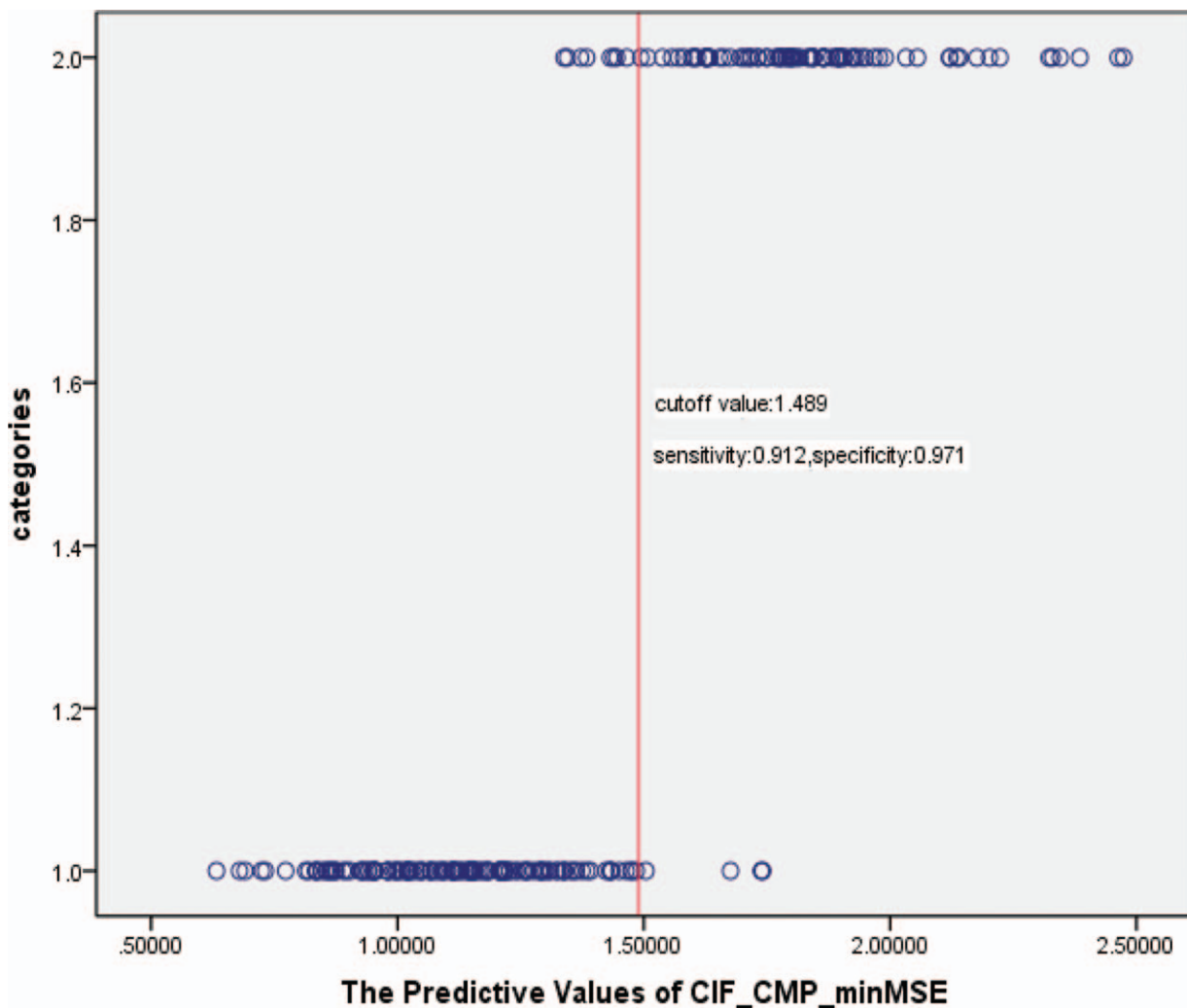

Figure 2. The scatter diagram of the predictive values of CIF-CMP-minMSE for predicting low- and high- grade ccRCC. ccRCC=clear cell renal cell carcinoma, CIF-CMP-minMSE=combined model of CIF-minMSE and CMP-minMSE.

Figure 3. The histogram of the predictive values of CIF-CMP-minMSE for predicting low- and high- grade ccRCC. ccRCC = clear cell renal cell carcinoma, CIF-CMP-minMSE = combined model of CIF-minMSE and CMP-minMSE.
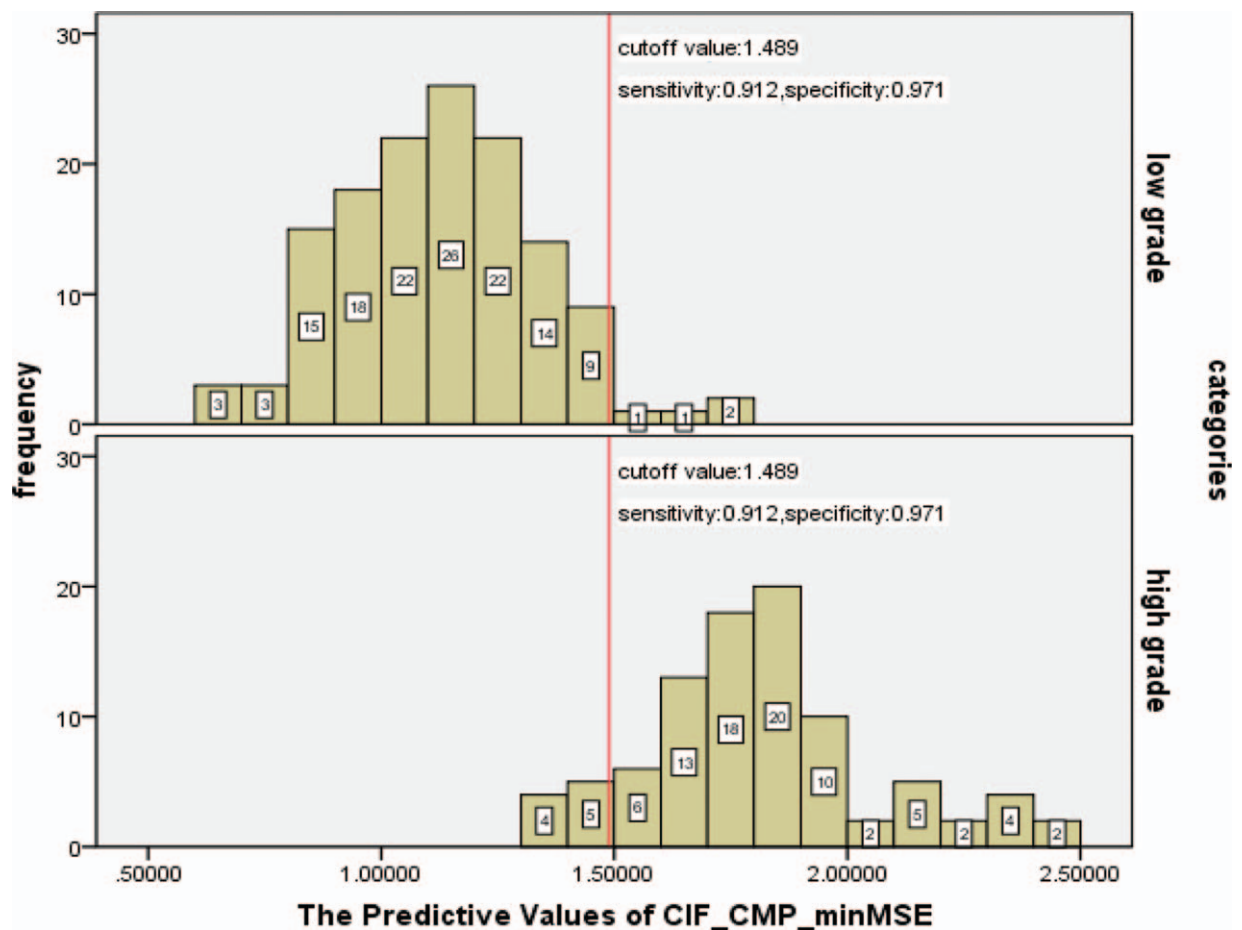
4. Discussion

In this study, 14 CIFs and 556 RFs were extracted from the 3-phase MDCT images of each ccRCC. Using the features selected from CIFs and RFs by Lasso regression, we got predictive equation of CIF-minMSE, CMP-minMSE, and PP-minMSE, respectively, in which each predictive feature had its own weight coefficient positive or negative. We proposed 5 predictive models composed by the selected CIFs and RFs to differentiate low-grade (WHO/ISUP grade 1 and 2) from high-grade (WHO/ISUP grade 3 and 4) ccRCC. On account of the AUC from large to small, the order of the 5 predictive models was CIF-CMP-minMSE (AUC: 0.986), CIF-PP-minMSE (AUC: 0.981), CIF-minMSE (AUC: 0.980), CMP-minMSE (AUC: 0.975), and PP-minMSE (AUC: 0.963). It was found that the RFs either extracted from CMP or PP, especially the former, were able to improve the accuracy rate of predicting the low- and high-grade ccRCC and the optimal predictive model was CIF-CMP-minMSE. Furthermore, among all the features, the feature X9—the maximum diameter of the largest axial section of ccRCC—was found having the maximum positive weight in predicting the WHO/ISUP grade of ccRCC.

Some previous studies had indicated the values of RFs extracted from CT or MRI images in the diagnoses, classifications, prognoses, and identifications of many tumors, such as the cancers of lung, rectum, breast, stomach, and brain.[29–32] The reasons speculated by researchers might be that the RFs were closely related to the internal structures of niduses and partly

Table 4

The results of the 5 predictive models in predicting the low- and high-grade of clear cell renal cell carcinoma (ccRCC).

Name of model	Cutoff value	Sensitivity (%)	Specificity (%)	Area of AUC
CIF-minMSE	1.451	94.5	92.6	0.980
CMP-minMSE	1.433	94.5	91.9	0.975
PP-minMSE	1.486	86.8	93.4	0.963
CIF-CMP-minMSE	1.489	91.2	97.1	0.986
CIF-PP-minMSE	1.491	90.1	95.6	0.981

ccRCC = clear cell renal cell carcinoma, CIF = conventional image feature, CIF-CMP-minMSE = the combined model of CIF-minMSE and CMP-minMSE, CIF-minMSE = minMSE of CIFs, CIF-PP-minMSE = the combined model of CIF-minMSE and PP-minMSE, CMP = cortico-medullary phase of kidney, CMP-minMSE = minMSE of CMP, minMSE = minimum mean squared error model, PP = parenchyma phase of kidney, PP-minMSE = minMSE of PP.
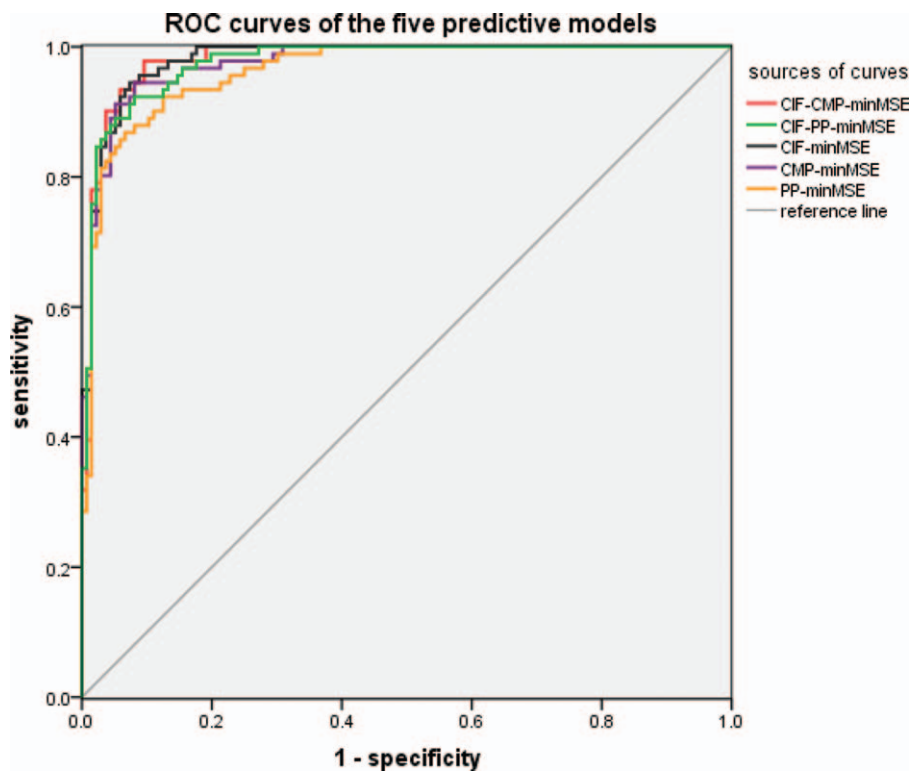
Figure 4. The centralized display of the ROC curves of the 5 predictive models. ROC = receiver operating characteristic.

reflected the heterogeneities of tumors. About ccRCC, there were also some studies on RFs could be found. Kierans et al[33] found that high-grade ccRCC had significantly higher skewness of GLH and correlations of GLCM on preoperative magnetic resonance (MR) diffusion-weighted imaging (DWI) than that of low-grade ccRCC, respectively. Lubner et al[34] studied 157 patients with RCC and drew a conclusion that the entropy, mean of positive pixels, and standard deviation of the pixel distribution of GLH on CT images were associated with tumor histologic types, nuclear grades, and outcomes. Ding et al[35] calculated texture-score using 4 RFs (RunLengthNonuniformity, Contrast, GrayLevel-Nonuniformity and 0.025Quantile) selected from 184 RFs extracted from MDCT images of each ccRCC and found the texture-score was valuable in the preoperative discrimination of the low from high grade ccRCC. Compared to the previous researches, some similar results could be got by this study, however, the larger numbers of patients (227 cases) and RFs (556 features) were studied and the outdated Fuhrman grade system of ccRCC was substituted by WHO/ISUP grade system adopted by ISUP after March 2012. Among the AUCs of the 5 models, we found the AUC of CIF-CMP-minMSE was the largest one and that of CIF-PP-minMSE was the second. That was to say, when combined with CIF-minMSE, the RFs of MDCT images were conducive to the higher rate of correctly recognizing the low and high grade ccRCC, and moreover, the RFs of CMP-minMSE were more valuable than that of PP-minMSE. However, we also found, when used alone, the AUC of CIF-minMSE was larger than that of CMP-minMSE or PP-minMSE. That was to say, the CIFs were more valuable than RFs of CMP or PP in predicting the grade of ccRCC individually.

Among all the features in this study, the maximum diameter of the largest axial section of ccRCC was found having the maximum positive weight in predicting the grade of ccRCC and

its cutoff value was 6.15 cm, with a sensitivity of 0.901, a specificity of 0.963, and an AUC of 0.975. The similar results could also be found in some other studies. In Kierans' study,[33] the means of the tumor size of low and high grade ccRCC were 3.49 ± 1.57 cm and 6.94 ± 2.93 cm, respectively, and their difference was statistical significant. Frank and Zhang et al[36,37] also found the tumor size of ccRCC was positively correlated with the nuclear grade of tumor, with 1 cm increaser in diameter of tumor the possibility of high grade increased by 32%. The reason why the significant difference appeared between the tumor sizes of low- and high-grade ccRCC is not confirmed, the speculated reason needing further prove may be that the tumor cells will become more and more malignant with the tumor growth.

There were several limitations in this study. First, this study was a single-center retrospective research, and the results need further validation from multi-center samples. Second, due to the different shape of each patient, the tube voltage and milliampere second of each CT examination were not identically. And, in all patients, 204 cases were examined by a 64 multi-detector CT scanner, the remained 23 cases were examined by a 256-multidetector CT scanner. Because of this, the measurement errors might increase during extracting RFs. Third, the RFs extracted from the maximum axial section of tumors did not entirely reflect the texture structures of the 3-dimensional tumor, which should be further studied in the future. Fourth, there was no independent validation cohort in this study to evaluate the overfitting of these models. Fifth, the sample size of this study is still some small, and more cases need to be added in the future.

5. Conclusions

In this study, we presented the whole procedure of the analysis about massive RFs. According to Lasso regression, we

constructed 5 predictive models for discerning low- and high-grade ccRCC and proved the model of CIF-CMP-minMSE was the optimal predictive model. When combined with CIFs, the RFs extracted from MDCT images could contribute to the larger AUC of the predictive model. But, when used alone, the CIFs were more valuable than RFs. Nevertheless, among all the features, the CIF feature X9—the largest diameter of the maximum axial section of ccRCC—had the largest positive weight in predicting the grades of ccRCC.

Acknowledgments

Author contributions

Conceptualization: Xiaopeng He, Hanmei Zhang, Fugang Han, Bin Song.
Data curation: Xiaopeng He, Tong Zhang.
Formal analysis: Hanmei Zhang, Tong Zhang.
Methodology: Hanmei Zhang, Fugang Han, Bin Song.
Project administration: Xiaopeng He, Bin Song.
Supervision: Bin Song.
Validation: Tong Zhang.
Writing – original draft: Xiaopeng He.
Writing – review & editing: Xiaopeng He, Bin Song.

References

[1] Siegel RL, Miller KD, Jemal A. Cancer statistics, 2018. CA Cancer J Clin 2018;68:7–30. Doi: 10.3322/caac.21442.

[2] Barata PC, Rini BI. Treatment of renal cell carcinoma: current status and future directions practical implications for continuing education. CA Cancer J Clin 2017;67:507–24. Doi: 10.3322/caac.21411.

[3] Delahunt B, Srigley JR, Montironi R, et al. Advances in renal neoplasia: recommendations from the 2012 international society of urological pathology consensus conference. Urology 2014;83:969–74. Doi: 10.1016/j.urology.2014.02.004.

[4] Moch H, Cubilla AL, Humphrey PA, et al. The 2016 WHO classification of tumours of the urinary system and male genital organs—part A: renal, penile, and testicular tumours. Eur Urol 2016;70:93–105. Doi: 10.1016/j.eururo.2016.02.029.

[5] Verine J, Colin D, Nheb M, et al. Architectural patterns are a relevant morphologic grading system for clear cell renal cell carcinoma prognosis assessment: comparisons With WHO/ISUP grade and integrated staging systems. Am J Surg Pathol 2018;42:423–41. DOI: 10.1097/PAS.0000000000001025.

[6] Dagher J, Delahunt B, Rioux-Leclercq N, et al. Clear cell renal cell carcinoma: validation of World Health Organization/International Society of Urological Pathology grading. Histopathology 2017;71:918–25. Doi: 10.1111/his.13311.

[7] Delahunt B, McKenney JK, Lohse CM, et al. A novel grading system for clear cell renal cell carcinoma incorporating tumor necrosis. Am J Surg Pathol 2013;37:311–22. Doi: 10.1097/PAS.0b013e318270f71c.

[8] Kuthi L, Jenei A, Hajdu A, et al. Prognostic factors for renal cell carcinoma subtypes diagnosed according to the 2016 WHO renal tumor classification: a study involving 928 patients. Pathol Oncol Res 2017;23:689–98. Doi: 10.1007/s12253-016-0179-x.

[9] Hes O, Compérat EM, Rioux-Leclercq N, et al. The 2012 ISUP Vancouver and 2016 WHO classification of adult renal tumors: changes for common renal tumors. Diagnostic Histopathol 2016;22:41–6. Doi: 10.1016/j.mpdhp.2016.01.003.

[10] Steffens S, Roos FC, Janssen M, et al. Clinical behavior of chromophobe renal cell carcinoma is less aggressive than that of clear cell renal cell carcinoma, independent of Fuhrman grade or tumor size. Virchows Arch 2014;465:439–44. Doi: 10.1007/s00428-014-1648-9.

[11] Delahunt B, Cheville JC, Martignoni G, et al. The International Society of Urological Pathology (ISUP) grading system for renal cell carcinoma and other prognostic parameters. Am J Surg Pathol 2013;37:1490–504. Doi: 10.1097/PAS.0b013e318299f0fb.

[12] Chae H-D, Park CM, Park SJ, et al. Computerized texture analysis of persistent part-solid ground-glass nodules: differentiation of preinvasive lesions from invasive pulmonary adenocarcinomas. Radiology 2014;273:285–93. Doi: 10.1148/radiol.14132187.

[13] Gillies RJ, Kinahan PE, Hricak H. Radiomics: images are more than pictures, they are data. Radiology 2016;278:563–77. Doi: 10.1148/radiol.2015151169.

[14] Meskawi M, Sun M, Ismail S, et al. FG has no added value in prediction of mortality after partial and radical nephrectomy for chromophobe renal cell carcinoma patients. Mod Pathol 2013;26:1144–9. Doi: 10.1038/modpathol.2012.230.

[15] Haider MA, Vosough A, Khalvati F, et al. CT texture analysis: a potential tool for prediction of survival in patients with metastatic clear cell carcinoma treated with sunitinib. Cancer Imaging 2017;17:1–9. Doi: 10.1186/s40644-017-0106-8.

[16] Avanzo M, Stancanello J, El Naqa I. Beyond imaging: the promise of radiomics. Phys Medica 2017;38:122–39. Doi: 10.1016/j.ejmp.2017.05.071.

[17] Ko ES, Kim JH, Lim Y, et al. Assessment of invasive breast cancer heterogeneity using whole-tumor magnetic resonance imaging texture analysis correlations with detailed pathological findings. Medicine 2016;95:1–8. Doi: 10.1097/MD.0000000000002453.

[18] Muglia VF, Prando A. Renal cell carcinoma: histological classification and correlation with imaging findings. Radiol Bras 2015;48:166–74. Doi: 10.1590/0100-3984.2013.1927.

[19] Zhang B, Tian J, Dong D, et al. Radiomics features of multiparametric MRI as new prognostic factors in advanced nasopharyngeal carcinoma. Clin Cancer Res 2017;23:4259–69. Doi: 10.1158/1078-0432.CCR-16-2910.

[20] Huang YQ, Liang CH, He L, et al. Development and validation of a radiomics nomogram for preoperative prediction of lymph node metastasis in colorectal cancer. J Clin Oncol 2016;34:2157–64. Doi: 10.1200/JCO.2015.65.9128.

[21] Giganti F, Marra P, Ambrosi A, et al. Pre-treatment MDCT-based texture analysis for therapy response prediction in gastric cancer: comparison with tumour regression grade at final histology. Eur J Radiol 2017;90:129–37. Doi: 10.1016/j.ejrad.2017.02.043.

[22] Huhdanpaa H, Hwang D, Cen S, et al. CT prediction of the Fuhrman grade of clear cell renal cell carcinoma (RCC): towards the development of computer-assisted diagnostic method. Abdom Imaging 2015;40:3168–74. Doi: 10.1007/s00261-015-0531-8.

[23] Yu HS, Scalera J, Khalid M, et al. Texture analysis as a radiomic marker for differentiating renal tumors. Abdom Radiol 2017;42:2470–8. Doi: 10.1007/s00261-017-1144-1.

[24] Szczypinski PM, Strzelecki M, Materka A. MaZda—a software for texture analysis. Comput Meth Prog Bio 2009;94:66–76. Doi: 10.1109/isitc.2007.15.

[25] Strzelecki M, Szczypinski P, Materka A, et al. A software tool for automatic classification and segmentation of 2D/3D medical images. Nuclear Inst Methods Phys Res A 2013;702:137–40. 2013;702(2):137-140. Doi: 10.1016/j.nima.2012.09.006.

[26] Ji L, Ren Y, Liu G, et al. Training-based gradient LBP feature models for multiresolution texture classification. IEEE Trans Cybern 2018;48:2683–96. Doi: 10.1109/TCYB.2017.2748500.

[27] Xie J, Zhang L, You J, et al. Effective texture classification by texton encoding induced statistical features. Pattern Recognit 2015;48:447–57. Doi: 10.1016/j.patcog.2014.08.014.

[28] Ranstam J, Cook JA. LASSO regression. Br J Surg 2018;105:1348Doi: 10.1002/bjs.10895.

[29] Digumarthy SR, Padole AM, Lo Gullo R, et al. CT texture analysis of histologically proven benign and malignant lung lesions. Medicine 2018;97:1–6. Doi: 10.1097/MD.0000000000011172.

[30] Chamming's F, Ueno Y, Ferré R, et al. Features from computerized texture analysis of breast cancers at pretreatment MR imaging are associated with response to neoadjuvant chemotherapy. Radiology 2018;286:412–20. doi: 10.1148/radiol.2017170143. Doi: 10.1148/radiol.2017170143.

[31] Wang H, Guo XH, Jia ZW, et al. Multilevel binomial logistic prediction model for malignant pulmonary nodules based on texture features of CT image. Eur J Radiol 2010;74:124–9. Doi: 10.1016/j.ejrad.2009.01.024.

[32] Skogen K, Schulz A, Dormagen JB, et al. Diagnostic performance of texture analysis on MRI in grading cerebral gliomas. Eur J Radiol 2016;85:824–9. Doi: 10.1016/j.ejrad.2016.01.013.

[33] Kierans AS, Rusinek H, Lee A, et al. Textural differences in apparent diffusion coefficient between low- and high-stage clear cell renal cell carcinoma. Am J Roentgenol 2014;203:637–44. Doi:10.2214/AJR.14.12570.

[34] Lubner MG, Stabo N, Abel EJ, et al. CT textural analysis of large primary renal cell carcinomas: pretreatment tumor heterogeneity correlates with histologic findings and clinical outcomes. Am J Roentgenol 2016;207:96–105. Doi: 10.2214/AJR.15.15451.

[35] Ding J, Xing Z, Jiang Z, et al. CT-based radiomic model predicts high grade of clear cell renal cell carcinoma. Eur J Radiol 2018;103:51–6. Doi: 10.1016/j.ejrad.2018.04.013.

[36] Frank I, Blute ML, Cheville JC, et al. Solid renal tumors: an analysis of pathological features related to tumor size. J Urol 2003;170:2217–20. Doi: 10.1097/01.ju.0000095475.12515.5e.

[37] Zhang C, Li X, Hao H, et al. The correlation between size of renal cell carcinoma and its histopathological characteristics: a single center study of 1867 renal cell carcinoma cases. BJU Int 2012;110(11 B):481–5. Doi: 10.1111/j.1464-410X.2012.11173.x.